Article

Calorimetric Testing of Solar Thermal Absorbers for High Vacuum Flat Panels

Carmine D'Alessandro[1,2,3], Davide De Maio[1,2,3], Antonio Caldarelli[1,2], Marilena Musto[1,2], Francesco Di Giamberardino[3], Matteo Monti[3], Teresa Mundo[3], Emiliano Di Gennaro[4,2], Roberto Russo[2*] and Vittorio G. Palmieri[3]

1. Industrial Engineering Department, University of Napoli "Federico II", Napoli, 80125, Italy; dalessandro@tvpsolar.com (C.A.); demaio@tvpsolar.com(D.M.); antonio.caldarelli@na.isasi.cnr.it(A.C.); marmusto@unina.it(M.M.);
2. National Research Council, Institute of Applied Science and Intelligent Systems, Unit of Naples, 80131, Italy
3. TVP Solar SA, 10 rue du Pré-de-la-Fontaine ZIMEYSA 1242 Satigny (GE), Switzerland; digiamberardino@tvpsolar.com(F.G.); monti@tvpsolar.com(M.M.); mundo@tvpsolar.com(T.M.); palmieri@tvpsolar.com(V.P.)
4. Physics Department, University of Napoli "Federico II", Napoli, 80126, Italy; emiliano.digennaro@unina.it(E.G.)

* Correspondence: Roberto.Russo@na.isasi.cnr.it

Abstract: Among solar thermal collectors, the evacuated flat panel is emerging as a reference technology for operation at higher temperatures of up to 200 °C with an increased annual energy production owing to both direct and diffuse light capture. Accurate measurements of the optical properties of the selective absorbers used in such devices are key for a reliable estimation of the overall performance. These optical properties must be measured under high vacuum at high temperatures, conditions under which the panels are meant to operate. In this study, we accurately measured these properties using a calorimetric technique. The measurement procedure is based on a power balance equation for a flat sample suspended in a high-vacuum chamber with minimal thermal losses and is well adapted for this class of devices. Calorimetric measurements obtained under Sun and LED light revealed excellent reproducibility and good agreement with those obtained using traditional optical analysis at low temperatures in air. When extended up to the absorber stagnation temperature, which often exceeds 300 °C, the calorimetric measurements started to deviate from the optical measurements, indicating the importance of measuring under the operating conditions.

Keywords: Selective Solar Absorber; Solar Absorptance; Thermal Emittance; Evacuated Flat Panel; Calorimeter; High Vacuum Flat Panel; Solar Simulator

1. Introduction

Solar thermal collectors may play a key role in the decarbonisation process of heat production. Worldwide, there is a huge demand for industrial process heat, and several technologies are available to convert the Sun's light power on a large scale (Farjana et al., 2018; Ismail et al., 2021). The adoption of a proper receiver architecture mainly depends on the operating temperature, and ranges from flat panels to concentrating power plants (Gorjian et al., 2020; Tian and Zhao, 2013). All possible collector designs can be distinguished by the grade of the sun's light concentration, type of tracking system, insulation, and shape of the absorber (Pranesh et al., 2019; Tian et al., 2018; Vengadesan and Senthil, 2020; Verma et al., 2020). Even if the available types of collectors are extremely diverse, they all share two main goals: maximisation of the sun's light conversion into heat and minimisation of thermal losses.

For temperatures of up to 200 °C, a novel architecture is emerging: a high vacuum flat plate (HVFP) collector hosting a planar absorber under high vacuum insulation (Buonomano et al., 2016). The presence of high vacuum in the panel represents the main difference between HVFP and evacuated flat panel (EFP) since EFP can also work at low-medium vacuum pressure (Benz and Beikircher, 1999). For HVFP collectors, convection losses are practically eliminated, and only conduction and radiation losses remain in addition to optical losses. In 2018, Moss et al. tested a small-scale prototype, showing that a reduction in the internal pressure to below 5x10⁻³ mbar minimized the thermal

conduction of residual gases to a negligible level. They also showed that HVFPs can potentially guarantee a larger quantity of annually converted energy by more than 60% with respect to the evacuated tube architecture owing to a wider acceptance angle, a better collection of the diffuse light and a larger fill factor of the gross area. Commercial devices have been introduced to the market (Benvenuti, 2013; TVP Solar SA, 2017), and a recent study reported on the experimental results from a 50 m² plant using TVP solar SA panels during a four-month testing period (Gao et al., 2020). An efficiency of 50% was achieved at a fluid temperature of 150 °C above ambient temperature, setting a record for solar thermal collectors.

When conduction losses due to the inevitable point of contact of the absorber with the panel envelope are minimised, the performance of this type of solar panel is mainly defined by the optical properties of the absorber because heat conduction through residual gases is negligible owing to the high vacuum (pressure below 10⁻⁴ mbar). Therefore, establishing the optical properties can lead to a reliable calculation of the overall panel efficiency with a high precision.

In this study, we focus on a procedure for measuring the optical properties of the absorber, namely, the solar light absorptance and thermal emittance. Equations 1 and 2 express the absorptance (or spectrally averaged solar absorptivity) α_{Sun} and thermal emittance (or spectrally averaged emissivity) ε_{abs}, respectively. They are a function of the spectral absorptivity α_λ integrated over the Sun's spectrum G_{Sun} in the first case and of the spectral emissivity ε_λ integrated over black body emission E_{bb} (see Eq. 3) in the second case:

$$\alpha_{Sun} = \frac{\int_{0.3\,\mu m}^{2.5\,\mu m} G_{Sun}(\lambda)\alpha_\lambda d\lambda}{\int_{0.3\,\mu m}^{2.5\,\mu m} G_{Sun}(\lambda)d\lambda} \tag{1}$$

$$\varepsilon_{abs}(T_{abs}) = \frac{\int_{2.0\,\mu m}^{100\,\mu m} E_{bb}(\lambda, T_{abs})\varepsilon_\lambda d\lambda}{\sigma T_{abs}^4} \tag{2}$$

$$E_{bb}(\lambda, T_{abs}) = \frac{2\pi hc^2}{\lambda^5} \cdot \frac{1}{\exp\left(\frac{hc}{\lambda k_B T_{abs}}\right) - 1} \tag{3}$$

where λ is the electromagnetic wavelength, T_{abs} is the absorber's temperature, c is the speed of light, h, σ and k_B are Planck's, Stefan's, and Boltzmann's constants, respectively.

Under the hypothesis of steady-state conditions, the Kirchhoff law of radiation states that $\alpha_\lambda = \varepsilon_\lambda$; in addition, in the presence of an opaque surface, i.e., no transmissivity, α_λ and ε_λ are complementary to reflectivity:

$$\alpha_\lambda = \varepsilon_\lambda = 1 - \rho_\lambda \tag{4}$$

As a consequence, α_λ and ε_λ are traditionally determined by optical measurements of the absorber reflectivity ρ_λ, where the subscript λ indicates that they are wavelength dependent quantities.

The measurement of ρ_λ is performed with reflectometers for the visible to the near infra-red (IR) wavelength range and Fourier Transform Infra-Red (FTIR) spectrophotometers for the near IR to the far IR. Both instruments measure the reflection from a sample under illumination by a controlled light beam as a function of the radiation wavelength. Measurements are usually conducted at room temperature, so the dependence of ε_{abs} on T_{abs} in Eq. 2 is only due to the temperature dependence of Plank's law (see Eq. 3), assuming ε_λ is constant across all temperatures. Considering ε_λ to be temperature independent inevitably leads to some approximations. Echániz et al. measured ε_λ for a solar absorber (based on Si, N, Mo over Ag-coated stainless steel) at various T_{abs}, from 250 °C to 600 °C and results of calculations of the thermal emittance $\varepsilon_{abs}(T_{abs})$ increased by up to 8% if compared with values extrapolated from ε_λ measurements at room temperature (Echániz et al., 2015). Similarly large discrepancies were reported also in other works on multi-layered coatings in the same temperature range (Jyothi et al., 2017; Niranjan et al., 2021).

Moreover, when measuring thin-film structures at high temperatures in air, an oxidation process may occur, which can affect the optical properties of the film. For this reason, when the absorber inside a solar collector works under high vacuum at high temperatures, measurements of the optical properties should be performed under the same conditions. Some research groups have developed instruments capable of measuring samples at high temperatures under vacuum (Le Baron et al., 2019; Mercatelli et al., 2015). However, these methods are quite complicated and expensive. Simpler

and less expensive methods would be very useful in assessing the optical properties of selective absorbers developed for working at high operating temperatures in HVFPs (De Maio et al., 2021a, 2021b).

When measuring under high vacuum, a calorimetric approach using a power balance equation can be used effectively for measuring α_{Sun} and ε_{abs} if controlled boundary conditions exist. The idea of a calorimetric measurement was already used in 1978 in testing selective coatings of metallic substrates (Willrath and Gammon, 1978). More recently, in 2015, Kreamer et al. proposed a calorimetric device for measuring α_{Sun} and the thermal emittance of both sides of a selective solar absorber, ε_{abs} and ε_{sub}, respectively (Kraemer et al., 2015). What neither of the two previous calorimetric testing methods can provide is tests of the absorber under sunlight.

In this work, we describe a novel device for calorimetric measurements of solar absorptance and the effective thermal emittance of highly selective flat absorbers under high vacuum. The test equipment was a panel-like high vacuum envelope designed for outdoor testing, direct exposure to sunlight, and indoors testing using an LED-based solar simulator (D'Alessandro et al., 2021). This allows for a determination of the thermal emittance and solar absorptance of the selective solar absorber up to the stagnation temperature with high accuracy.

2. Experimental set-up

The test equipment was aimed at reproducing a HVFP as closely as possible. In Fig. 1(a), the device configuration for outdoor testing is depicted. It consisted of a rectangular stainless steel vacuum chamber closed by a dismountable cover glass. A vacuum seal was obtained using a Viton O-Ring hosted in a groove on the chamber flange, which was directly compressed by the glass plate. Low pressure in the chamber was guaranteed by a pumping system composed of primary and turbo-molecular pumps connected in series. Flat absorber samples (dark blue surface in the picture), 140 mm × 150 mm, were placed inside the vacuum chamber and suspended by four stainless steel springs placed at the two opposite long edges of the sample. The dimensions of the sample and chamber were such that they reproduced the unit cell of an actual TVP Solar SA panel. In this panel, an array of holes was present in the full-scale absorber to allow metal pins to support the glass against atmospheric pressure. The vertical and horizontal pitches of the array were 140 mm and 150 mm, respectively. Therefore, the aim of this equipment was to test unit cell absorber samples in an environment as close as possible to that of the entire panel.

The pressure was measured during each test using a vacuum gauge (PKR 251, Pfeiffer). The temperatures of the absorber, cover glass, and chamber walls were measured using K-type thermocouples and read out using a USB module (National Instruments 9211). The glass and chamber temperature sensors were placed on the vacuum side so that the external air convection, natural or forced, did not affect the measurements. An additional thermocouple was crimped to a lug and screwed to the central hole of the sample using an M3 stainless steel bolt.

The entire system (vacuum chamber, pumping system, measurement probes, and electronics) was mounted on a trolley for outdoor testing, as shown in Fig. 1(a). This trolley was equipped with a tiltable support consisting of two slotted rods manually fixed by two screws to set the vacuum chamber at an angle with respect to the vertical. A meridian and pyranometer were attached parallel to the chamber to check the angle of the latter and to measure the intensity of the solar irradiation incident over time, respectively. The pyranometer used was a thermopile-type from Apogee, with a response time of 0.5 s, a measurement repeatability of less than 1%, and a calibration uncertainty of 5%. In addition, a second pyranometer (CMP11 secondary standard pyranometer from Knipp&Zonen) with a lower uncertainty of 1% and a longer response time of 5 s was used to normalise the average value of the first pyranometer. The measurements from the sensors (thermocouples, pressure gauge, and pyranometer) were recorded in a 1 s time interval.
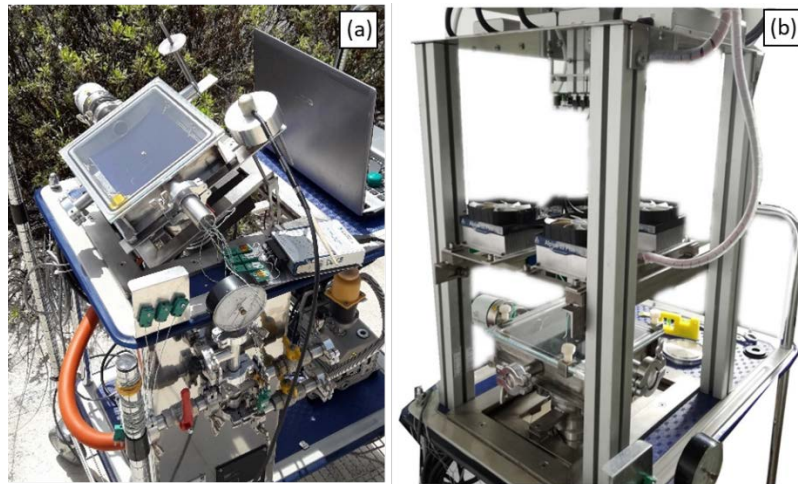
Figure 1. Experimental set-up for calorimetric testing in outdoor (a) and indoor (b) configuration. For outdoor testing the support positions of the chamber are tilted perpendicular to the Sun's beam. For indoor tests an LED light source (D'Alessandro et al., 2021) illuminates the chamber.

For indoor testing, the chamber was set horizontally and illuminated using an LED light source, as described in a previous paper (D'Alessandro et al., 2021). Figure 1(b) shows the LED system with its supporting structure when placed on the same trolley. The system was composed of four LED lamps arranged along the vertices of a square parallel to the plane of the sample, with each LED lamp attached to a modified CPU cooler. It is possible to separately adjust the position of each lamp in the horizontal plane, whereas the vertical distance can only be set for the four lamps together. The intensity is controlled by a proportional voltage signal driving the LEDs power supplies, and the incident light power density reaching the chamber can be fine-tuned between 400 Wm^{-2} and 1.3 kWm^{-2}. This allowed for an estimation of the incident power on the sample surface with a 1% accuracy (D'Alessandro et al., 2021). As LEDs emit light only in the range 0.3 – 0.7 μm (CREE, 2014), indoor testing of absorptance is limited to this spectral range, whereas measurements with the complete Sun spectrum are performed outdoors.

3. The Calorimetric Equation

The typical calorimetric equation for a system under study can be written as follows:

$$m_{abs} c_p(T) \frac{dT_{abs}}{dt} = \dot{Q}_{heating} - \varepsilon_e(T) \sigma A_{abs}(T_{abs}^4 - T_{amb}^4) - K_{all}(T_{abs} - T_{amb}) \qquad (5)$$

where m_{abs}, $c_p(T)$, T_{abs} and A_{abs} are the mass, temperature-dependent heat capacity, temperature, and absorber surface, respectively. $\dot{Q}_{heating}$ is a positive contribution to the absorber's temperature derivative dT_{abs}/dt owing to the absorbed light. $\varepsilon_e(T)$ is the effective emittance that regulates the radiative exchange with the surrounding surfaces at ambient temperature T_{amb} and depends on the thermal emittance, shape, and relative position of all surfaces of the cavity (Howell et al., 2021). In our system ε_e can be calculated using a model of parallel plates with thermal emittances ε_1 and ε_2,

$$\varepsilon_e = \frac{1}{\frac{1}{\varepsilon_1} + \frac{1}{\varepsilon_2} - 1} \qquad (6)$$

Finally, K_{all} is the parameter that includes all other heat losses, and in the following sections, its contribution to the calorimetric equation is calculated and demonstrated to be negligible.
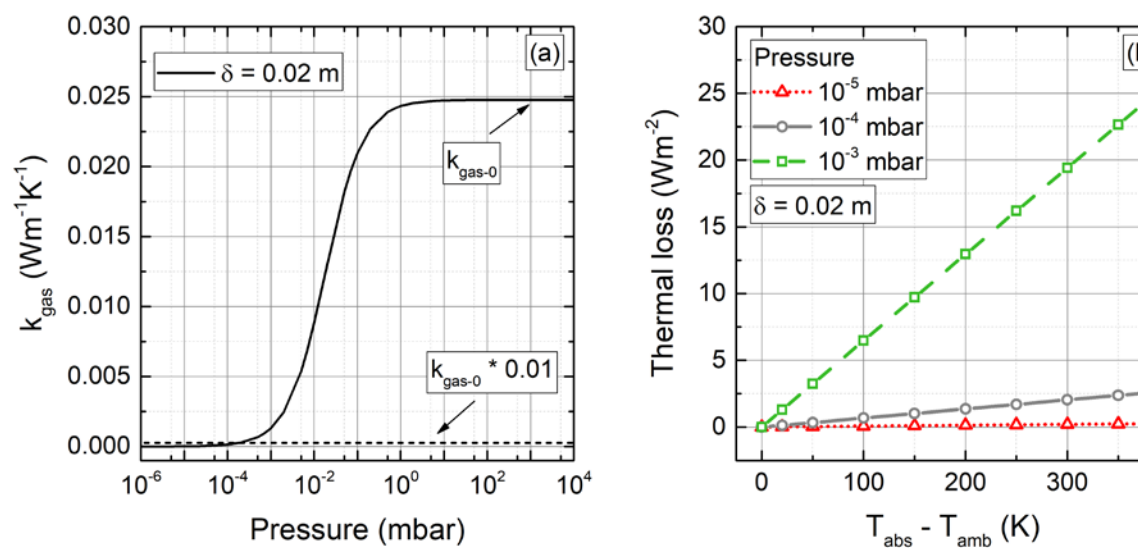
3.1 Thermal loss due to residual gas

The first term that contributes to K_{all} is the thermal conductivity k_{gas}. The test equipment included a pumping system capable of maintaining the chamber under high vacuum. Under such conditions, thermal losses via residual gases are generally negligible, but some quantitative considerations must be made (Arya et al., 2018a, 2018b). Equation (7) describes the thermal conductivity k_{gas} of the residual gases as a function of the Knudsen number Kn.

$$k_{gas} = \frac{k_{gas-0}}{1 + 2\beta Kn} \tag{7}$$

Kn is a dimensionless parameter defined as the ratio between the mean free path of the gas particles and the characteristic size δ of the chamber. When the gas temperature and δ are constant, Kn is inversely proportional to the pressure. k_{gas-0} is the thermal conductivity of air at ambient pressure, and β is a parameter which depends on the nature of the residual gases and the accommodation fraction of the surfaces (Dushman et al., 1949). In Fig. 2(a), the thermal conductivity of residual gases is reported as a function of pressure for $\delta = 0.02$ m, which is representative of the distance between the sample and the walls of the chamber facing it. Between a pressure of 10^3 mbar and 10 mbar, there is no change in k_{gas}. In this range, pressure alteration causes variations in particle collisions per unit volume, which is counterbalanced by variations in the mean free path (continuous matter domain).

In the range of $10^{-4} - 10$ mbar, k_{gas} decreases with pressure, and for a pressure of 10^{-4} mbar and below, k_{gas} remains below 1%. Such a strong reduction in pressure leads to a condition in which the mean free path of particles becomes smaller than δ; thus, the number of collisions between particles is lower than that between particles and walls (molecular domain) (Beikircher et al., 1995). It is possible to calculate thermal losses in terms of Wm^{-2} as k_{gas} times the temperature difference between the absorber and the environment, $T_{abs} - T_{amb}$, divided by δ. Figure 2(b) shows the resulting loss for three internal pressures of 10^{-5}, 10^{-4} and 10^{-3} mbar with $\delta = 0.02$ m. When the pressure is equal to or below 10^{-4} mbar the losses do not exceed 5 Wm^{-2} even for values of $T_{abs} - T_{amb}$ as high as 400 K. In contrast, at a pressure of 10^{-3} mbar the losses are significantly higher, as the dependence of k_{gas} on pressure is not linear. The pressure of 10^{-4} mbar is therefore a threshold that guarantees only a few Wm^{-2} of losses, which is negligible when compared to the typical 1 kWm^{-2} irradiance in solar applications. During all experimental runs, the internal pressure of the chamber was always below such threshold, and $T_{abs} - T_{amb}$ never exceeded 300 K, ensuring that any contribution to K_{all} due to residual gases could be neglected.

Figure 2. Effect of the pressure of the residual gas inside the vacuum chamber on the thermal conductivity k_{gas}. (a) k_{gas} is expressed in Wm^{-1}K^{-1} and is reported as a function of pressure for the characteristic length $\delta = 0.02$ m. (b) Thermal losses due to residual gases are reported in Wm^{-2} relative to $\delta = 0.02$ m and for the three pressure levels of 10^{-5}, 10^{-4} and 10^{-3} mbar as a function of $T_{abs} - T_{amb}$.

## 3.2 Thermal loss due to supporting springs

An additional contribution to K_{all} to be considered is the contact between the sample and the stainless steel supporting springs. In the worst-case scenario, this contact was perfect, and the ends of the two springs were at T_{abs} and T_{amb}, respectively, dissipating heat via conduction and radiative emission toward the chamber walls. The following differential Eq. (8) governs the temperature distribution over the length of a straight wire under steady-state conditions and circular cross-sections (Masuda and Higano, 1985):

$$\frac{d^2T}{dx^2} = \frac{4\varepsilon_w\sigma}{k_w D_w}(T^4 - T_{amb}^4) \tag{8}$$

where T is the temperature of the wire at the spatial coordinate x, k_w, D_w and ε_w are the wire's thermal conductivity, diameter, and thermal emittance, respectively. Assuming contact with the sample at $x = 0$, the corresponding heat loss through the wire is:

$$\dot{Q}_s = \frac{\pi}{4}D_w^2 k_w \frac{dT}{dx}\bigg|_{x=0} \tag{9}$$

Using the finite element method, we numerically solved the differential Eq. 8 and the resulting temperature distribution is shown in Fig. 3(a) as $T - T_{amb}$ (with D_w = 0.45 mm, ε_{wire} = 0.15, k_w = 17 Wm^{-1}K^{-1}, T_{amb} = 303 K, and $T_{abs} - T_{amb}$ = 400 K). The distribution is roughly linear, meaning that the conduction mechanism is dominant over the radiative one. In Fig. 3(b) the thermal losses calculated by Eq. 9 are reported for the case of a 140 mm x 150 mm sample area and four supporting springs. The power losses are extremely low (below 1 Wm^{-2}), so the impact of the supporting springs is surely negligible and will not be accounted for in K_{all}.
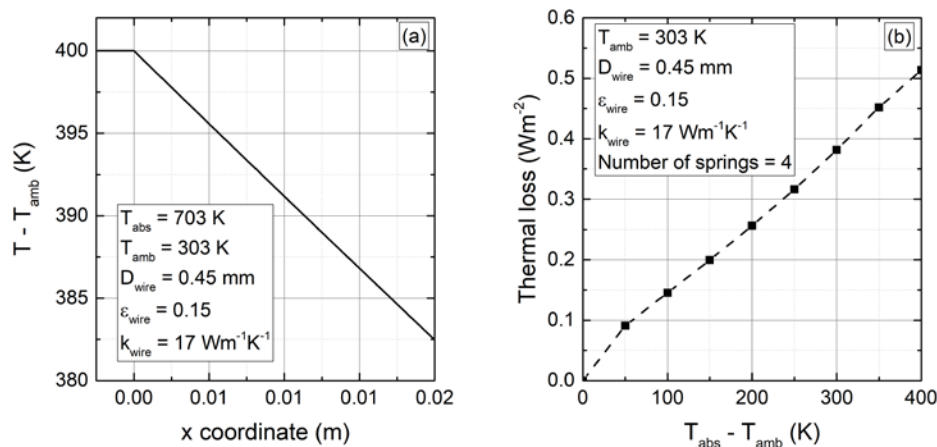
Figure 3. (a) Temperature distribution over the wire for $T_{abs} - T_{amb}$ = 400 K as a result of the differential Eq. 8 solved by a finite element method. (b) Thermal loss calculated by Eq. 9 is expressed in Wm^{-2} for four springs in perfect contact with the sample and chamber as a function of $T_{abs} - T_{amb}$. The surface referred to is an area of 140 x 150 mm^2 of the sample.

3.3 Thermal losses due to the presence of a thermocouple

The presence of a stainless steel bolt and nut attached to the absorber for fastening the thermocouple is an additional source of radiation loss to be considered. This could affect the tests because the thermal emittance and light absorptance are likely to differ with respect to the absorber under test. However, the total exposed surface was more

than two orders of magnitude lower than that of the investigated sample, and even if its radiative properties differed from those of the absorber, its contribution to K_{all} could be neglected. Therefore, the role of the bolt and nut is limited to its thermal capacitance, which is added to the thermal capacitance of the sample.

3.4 Formulation of the sample's calorimetric equation

Under the previous assumptions, the term K_{all} can be neglected, and the power-balance equation of the absorber can be rewritten as follows:

$$\frac{(m_{abs}c_{p_{abs}}+m_{th}c_{p_{th}})}{A_{abs}}\frac{dT_{abs}}{dt} = P_l\alpha_l\tau_g - \varepsilon_{eabs}(T)\sigma\left(T_{abs}^4 - T_g^4\right) - \varepsilon_{es}(T)\sigma(T_{abs}^4 - T_v^4) \qquad (10)$$

where m_{abs}, c_{pabs}, m_{th} and c_{pth} are the mass and specific heat of the absorber and the thermocouple fastening bolt and nut, respectively. A_{abs} is the sample surface area of the side exposed to the light source. P_l and α_l are the light power density incident on the glass closing the vacuum chamber and the spectrally averaged absorptivity of the sample, respectively. Depending on the adopted light source, P_l and α_l are specified as P_{Sun} and α_{Sun} in the case of outdoor testing and as P_{LED} and α_{LED} for indoor testing. τ_g and T_g are the light transmittance and the measured temperature of the glass, respectively. The product of P_l, α_l and τ_g defines the heating of the sample within the chamber.

Commercial flat absorbers are thin metal foils, typically aluminium or copper, coated on one side with a selectively absorbing coating. As the area of the coated side is equal to that of the uncoated side, A_{abs} represents both sides, and herein it is 140 mm × 150 mm. The thermal emission mechanism is modelled according to the Stefan-Boltzmann formulation, which expresses the radiative exchange by the difference between the fourth power of the two facing surface temperatures and an emittance parameter that considers such surfaces as non-ideal blackbodies. ε_{eabs} and ε_{es} are then the effective thermal emittance of the two sides of the sample. The first refers to the absorbing side facing the glass at T_g and the second to the substrate side facing the stainless steel chamber at temperature T_v.

Assuming $T_g = T_v$, one can rewrite the radiative terms in Eq. 10, which is proportional to the total effective thermal emittance, ε_{et}, as shown in Eq. 11. It obviously depends on the thermal emittance of each side of the sample and the walls of the chamber, being the sum of ε_{eabs} and ε_{es}.

$$\frac{(m_{abs}c_{p_{abs}}+m_{th}c_{p_{th}})}{A_{abs}}\frac{dT_{abs}}{dt} = P_l\alpha_l\tau_g - \varepsilon_{et}(T)\sigma\left(T_{abs}^4 - T_g^4\right) \qquad (11)$$

The previous simplification is acceptable because, during all runs, the maximum difference between T_g and T_v never exceeds 10 K, having an impact of less than 1% on the radiated power, and hence, also on the calculated ε_{et}.

Equation 11 is, therefore, the simplified power balance equation, which regulates the temperature of the sample T_{abs} over time t. This equation is used to calculate α_l and ε_{et} for the absorber sample because all other quantities can be readily measured.

4. Experimental calorimetric procedure

The calorimetric measurement procedure was divided into two steps: warm-up and cool-down. The first step involves exposing the sample to light through the cover glass and allowing its temperature to increase up to the stagnation temperature T_s. This temperature is the maximum achievable by the sample and occurs when the radiative emission equals the absorbed light in power. For all experimental runs, the sample was maintained at a stagnation temperature for at least 10 min. The second step, cool-down, consists of letting the sample cool by means of radiative emission, while it is shielded from any incident light by means of an aluminium shield placed on top of the cover glass.

The data analysis started with the cool-down. During this step, Eq. 11 has zero P_l, so ε_{et} can be calculated as the only unknown of the equation. Then, the warm-up is used to calculate α_l from Eq. 11 using ε_{et} from the cool-down.

In Fig. 4, all measured quantities during a single outdoor test are reported as a function of the relative time. The start of the warm-up phase was set at zero relative time. Before this moment, the sample was within the vacuum chamber with the system already oriented perpendicular to the Sun and the glass covered with an aluminium shield. Under this condition, the sample was at a temperature close to that of the vacuum chamber. When the shield was removed, the sample was exposed to solar irradiation, and the warm-up phase began (point A in Fig. 4). During this phase, T_{abs}, T_g and T_v increased with the internal pressure, never exceeding the threshold of 5×10^{-5} mbar during any run. Outdoor tests were conducted around solar noon on clear-sky days to minimise variations in solar irradiation. The maximum recorded variation in P_{Sun} over the entire warm-up phase was 5% of the initial value. The absorber temperature increases up to the stagnation temperature T_s, point B^s in Fig. 4. This condition was maintained for 10 min, and then, the glass was again covered with the aluminium shield, see point B, allowing the sample to cool to a temperature close to that of the vacuum chamber, point C.
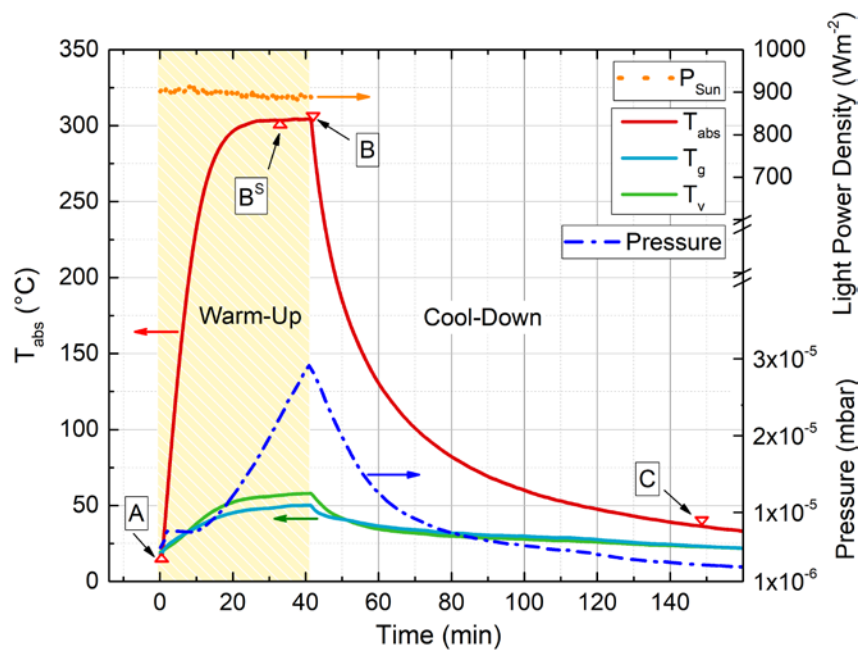

Figure 4. Time evolution of the sun light power density, chamber pressure, and temperature of different chamber elements during the outdoor experiment.

In Fig. 5, the time derivative of T_{abs} is reported as a function of relative time (a) and as a function of T_{abs} (b). According to Eq. 11, the maximum temperature derivative of the sample is expected at the start of the warm-up phase, as thermal losses are at a minimum. Experimentally, it is observed that the maximum temperature derivative occurs with a slight delay with respect to the sample illumination (point A* in Figs. 5(a) and 5(b)). This unavoidable effect, due to the presence of a thermocouple that slightly increases the thermal capacity of the sample, was taken into account when analysing the data. After reaching the maximum T_{abs}, the derivative had a progressively lower value, reaching zero at the stagnation temperature, point B^s. Therefore, the time interval with the sample at the stagnation temperature is characterised by a zero derivative of T_{abs} over time. Point B coincides with the illumination stopped by covering the glass with the aluminium shield; it defines the start of the cool-down phase, which has negative values for the T_{abs} derivative. Analogous to the warm-up phase, there is a delay for this derivative, and its absolute value reaches the maximum at point B* before decreasing very close to zero at point C in Fig. 5. When the absorber approaches the ambient temperature, the emitted power becomes very small, and therefore cool-down lasts much longer than the warm-up phase. The measurements were stopped when the absorber reached below 50 °C.

The experimental procedure for indoor testing was similar. The vacuum chamber was set horizontally, and the LED system was mounted on top of it with lamps facing the cover glass. Because of the transient time necessary for the stabilisation of the emitted light (D'Alessandro et al., 2021), the LEDs were switched on 30 min before the warm-up phase started, with the glass covered by the aluminium shield. Like the outdoor tests, the warm-up phase was started by removing the aluminium shield and was stopped by repositioning it.
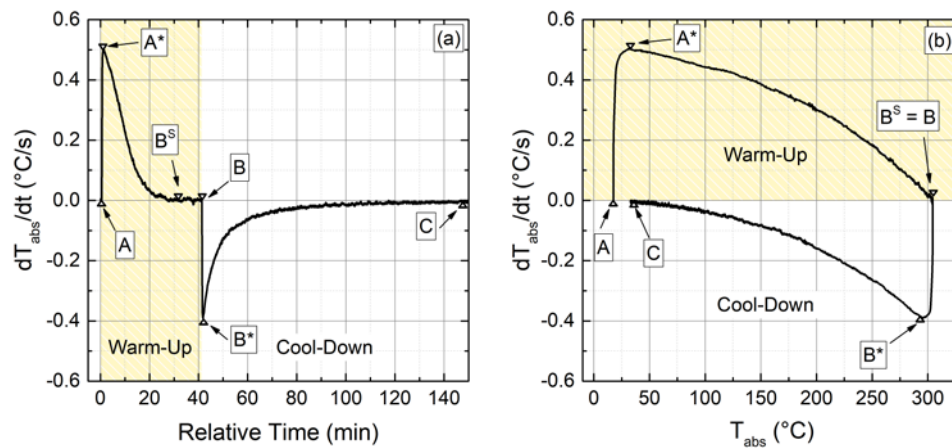
Figure 5. T_{abs} time derivative for an outdoor experiment is reported as function of relative time (a) and T_{abs} itself (b). The yellow background defines the warm-up, while the white indicates the cool-down. A 10-point moving average is used to reduce the noise.

5. Experimental Results

The experimental analysis was carried out on a sample cut from the Mirotherm® absorber from Alanod, the same absorber mounted in the TVP solar SA panels (Buonomano et al., 2016; Gao et al., 2020). It consisted of a 0.6 mm thick aluminium roll coated with a selective absorption layer on one side.

5.1 Optical Measurement Results

Optical measurements of the absorber reflectivity ρ_λ were performed for both the coated and uncoated sides of the absorber and the results were used to calculate the spectral absorptivity α_λ and emissivity ε_λ (Eq. 4). Calibrated references were used to normalize the reflectivity to 1.

Through Eqs. 1 and 2, we calculated the light absorptance and thermal emittance values. The latter can then be optically estimated for higher temperatures using Eq. 2 and the hypothesis that ε_λ does not change with temperature. Hereinafter, the subscript Opt will be adopted for light absorptance and thermal emittance obtained by optical measurements.

In Fig. 6(a), the spectral emissivity derived from the optical reflectivity measurements at room temperature is shown, $\varepsilon_{\lambda\text{-abs}}$ for the coated and $\varepsilon_{\lambda\text{-s}}$ uncoated side of the absorber. The analysis between 0.35 μm and 1.70 μm was performed using an integrating sphere from Ocean Optics equipped with a halogen lamp and connected to an Optical Spectrum Analyser through a fibre optic cable. Then, between 1.20 μm and 20.0 μm, a FTIR from Jasco equipped with a diffuse reflectivity accessory was used.

In the overlapping region (between 1.20 μm and 1.75 μm), the emissivity is the mean of the results of the two instruments. The coated side showed a good selectivity with high emissivity in the solar range (blue dashed line in Fig. 6(a)) which rapidly decreased at longer wavelengths. In contrast, the aluminium substrate has an emissivity $\varepsilon_{\lambda\text{-s}}$ (black solid line) lower than $\varepsilon_{\lambda\text{-abs}}$, particularly in the solar range, as there is no coating applied on the back of the absorber. In the same figure, the normalized solar spectrum incident on the terrestrial surface, standard ASTM G173-0 (orange area), and the normalized spectrum of the adopted LED lamps from CREE (violet area) are also reported.

The spectrally averaged absorptivity of the coated side was calculated using Eq. 1, using the corresponding light spectra with $\alpha_{\text{Sun-Opt}}$ and $\alpha_{\text{LED-Opt}}$ values of 0.933 and 0.947, respectively. The optical measurements were highly accurate and reproducible, and the uncertainty in α was estimated to be less than 0.003. The spectrally averaged emissivity $\varepsilon_{\text{abs-Opt}}$ and $\varepsilon_{\text{s-Opt}}$, relative to the spectral emissivity $\varepsilon_{\lambda\text{-abs}}$ and $\varepsilon_{\lambda\text{-s}}$, were calculated using Eq. 2 for several T_{abs} values (see Fig.

6(b)). $\varepsilon_{abs-Opt}$ is always higher than ε_{s-Opt} over the entire investigated temperature range of 50 °C - 300 °C, with a difference that ranges between 10% at T_{abs} = 50 °C and 40% at 300 °C.
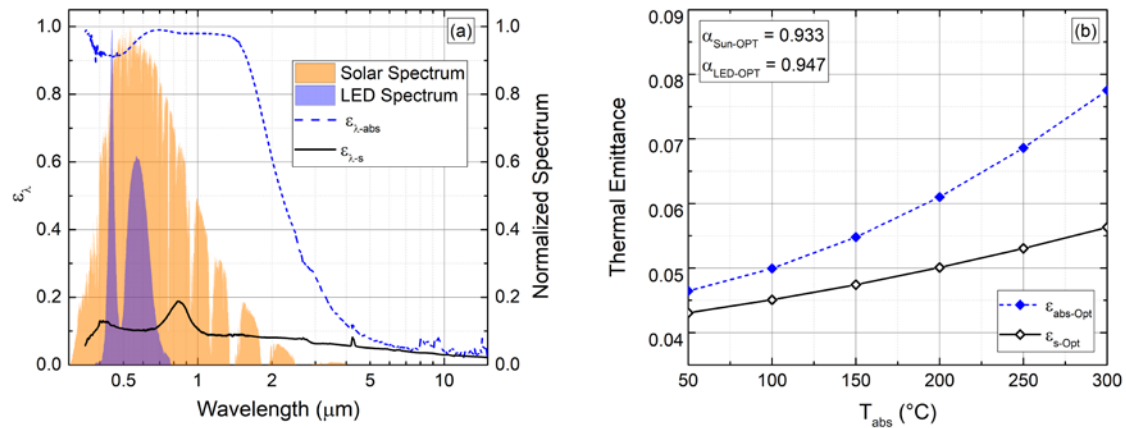
Figure 6. Results of the optical analysis are reported for both sides of the commercial absorber Mirotherm® from Alanod. (a) Spectral emissivity curve of coated, $\varepsilon_{\lambda-abs}$, and uncoated, $\varepsilon_{\lambda-s}$, side as measured by reflectometry and FTIR measurements at room temperature and shown as a function of wavelength. Also, normalized solar spectrum, ASTM G173-0 standard (orange area), and adopted LED spectrum (violet area) are reported. (b) Thermal emittance of coated, $\varepsilon_{abs-Opt}$, and uncoated, $\varepsilon_{sub-Opt}$, substrate side are estimated using Eq. 2 and reported as a function of T_{abs}. Absorptance is temperature independent with its values also reported in the figure.

5.2 Calorimetric measurements: total effective thermal emittance ε_{et}

Samples with an area of 210 cm² (140 × 150 mm) were weighed using a balance with a sensitivity of 0.001 g to precisely determine their mass (m_{abs}).

Estimations of α_l and ε_{et}, resulting from 12 calorimetric runs performed under different experimental conditions (6 performed outdoors and the other 6 indoors), are compared. Regarding the outdoor testing, the vacuum chamber walls were cooled by natural convection in all runs, from #1 to #6. For indoor testing, runs #1 and #2 refer to a P_{LED} close to 1 kWm⁻² with the chamber cooled by forced convection (electric fan); run #3 had a similar P_{LED} but without cooling: runs #4, #5 and #6 were performed without cooling too, but at reduced P_{LED}.

In Fig. 7(a), the ε_{et} temperature dependence, as a result from an analysis of the cooling-down phase (grey line) of a single run, is reported as function of T_{abs} along with the points B, B* and C. At the start of the cool-down phase, point B, the calculated ε_{et} is zero. At lower T_{abs}, as the cooling progresses, there is a rapid increase in the calculated ε_{et} up to point B*. This anomaly is due to the thermocouple fastening and is determined by the shape of dT_{abs}/dt in the B – B* interval, as seen in Fig. 5 and it was excluded from the analysis. In the following interval B* – C, the calculated ε_{et} is reduced together with T_{abs}, as was expected from the optical measurements, see Fig. 6(b). As the sample temperature approaches point C, the calculated ε_{et} fluctuates. This can be explained by the reduced derivative values of T_{abs} when the sample has a temperature close to the ambient one. The intrinsic noise of the thermocouple signal affects the estimation in this temperature region. To obtain an $\varepsilon_e(T)$ function that can be used to compare the data and calculate thermal radiative losses, a fitting procedure using a second order polynomial function ε_{etF} in the range B* – C was performed, see Fig. 7(a).

Figure 7(b) shows different $\varepsilon_{etF}(T)$ values resulting from runs #1 to #3 of the outdoor and indoor measurement campaigns (coloured lines). They all are in good agreement, and no trend can be extrapolated by comparing the indoor and outdoor results, implying that even if the test facility has different illumination, the resulting $\varepsilon_{etF}(T)$ is not affected. More experimental details regarding these external conditions are reported in the next section in Tables 1 and 2.

The six $\varepsilon_{etF}(T)$ results in Fig. 7(b) show a maximum difference of ±2.5% and ±4% with respect to the mean values in the absorber temperature range above and below 150 °C, respectively. Figure 7(b) also shows a comparison of the

optically determined total emittances ($\varepsilon_{abs\text{-}Opt}$ + $\varepsilon_{s\text{-}Opt}$ empty black diamonds) and the effective total thermal emittance $\varepsilon_{et\text{-}Opt}$ (black diamond with dots) calculated using Eq. 6, assuming a glass thermal emittance of 0.85 and a stainless steel thermal emittance of 0.13. At temperatures below 150 °C there is a substantial agreement between ε_{etF} of the six experiments and the sum $\varepsilon_{abs\text{-}Opt}$ + $\varepsilon_{s\text{-}Opt}$. With an increase in T_{abs}, the calorimetric results tend to be lower than the sum $\varepsilon_{abs\text{-}Opt}$ + $\varepsilon_{s\text{-}Opt}$. At T_{abs} = 200 °C, the sum $\varepsilon_{abs\text{-}Opt}$ + $\varepsilon_{s\text{-}Opt}$ starts to depart from the calorimetric values, and at T_{abs} = 300 °C it overestimates the total emittance by 0.01, i.e., by 9% of the calorimetric result, see Fig. 7(b). In contrast, the total effective emittance $\varepsilon_{et\text{-}Opt}$ calculated using Eq. 6 underestimates the calorimetric outcome over the entire investigated temperature range. This discrepancy reduces with temperature, ranging from 11% at T_{abs} = 50 °C to 8% at T_{abs} = 300 °C.

Neither the sum of the spectrally averaged emissivity of either side nor further correction by Eq. 6 can be used to obtain an accurate estimation of the actual effective total thermal emittance of the absorber when operating at a high temperature. The reason for this discrepancy may be a change in the spectral emissivity of the sample at high temperatures (Echániz et al., 2015).

The presented test equipment and procedure allow for the estimation of the actual thermal emittance of the absorber during operation in a HVFP without extending the optical measurements performed at room temperature to a high temperature.
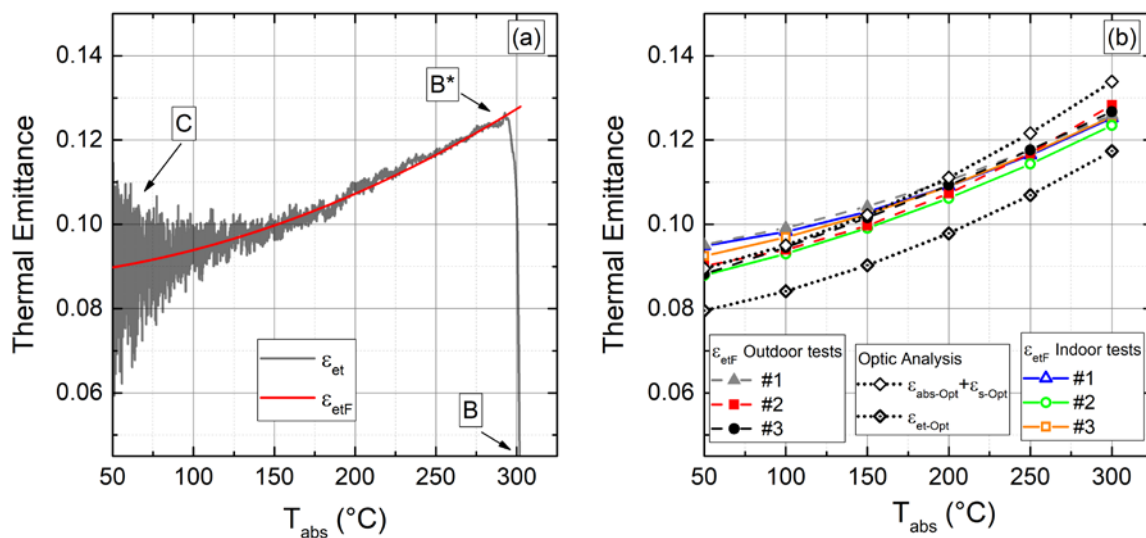
Figure 7. (a) An example of calorimetrically measured effective thermal emittance ε_{et} is reported together with the polynomial fitting curve ε_{etF} as a function of T_{abs}. (b) Polynomial fitting curves are reported as a function of T_{abs} for three indoor and three outdoor experiments together with the total thermal emittance derived by optical reflectivity measurements as the sum of $\varepsilon_{abs\text{-}Opt}$ and $\varepsilon_{s\text{-}Opt}$ (empty black diamonds), and as the effective emittance $\varepsilon_{et\text{-}Opt}$ calculated by Eq. 6 (black diamonds with central dot).

5.3 Calorimetric measurements: light absorptance

After the cool-down phase of each run, the warm-up phase was analysed to calculate α_l as the only unknown quantity of the calorimetric Eq. 11, adopting the $\varepsilon_{etF}(T)$ function resulting from the fitting of ε_{et} of the same test as the total effective thermal emittance. Using this approach, every run is a stand-alone experiment and does not correlate with the other results. The absorption mechanism of light, impinging on the glass cover, is modelled by the product of P_l, α_l and τ_g. The glass transmittance is measured as the ratio between the reading of the secondary pyranometer when exposed perpendicularly to the incident light underneath and above the glass. For both, the Sun and the LED light, the measured τ_g had the same value of 0.915.

Similar to ε_{et}, the calculated α_l from the warm-up phase also shows an anomaly due to the delayed response of the T_{abs} derivative. The delayed response impacts the measurement for no more than 20 °C and α_l is calculated only in the interval A* – B^s. For each indoor and outdoor run, the measured α_l in A* – B^s can be assumed to be constant with a

variation of ±1.5% around the mean value. α_{Sun} and α_{LED} resulting from the outdoor and indoor experimental campaigns are reported in the following Tables 1 and 2, respectively.

Table 1. Summary of six outdoor calorimetric experiments is reported. The table shows P_{Sun} measured at the start and end of the warm-up phase at points A* and B^s, the temperatures at the stagnation of the absorber, glass, and vacuum chamber, T_s, T_g and T_v, respectively. $\alpha_{Sun-Opt}$ and α_{Sun} for each test are reported. α_{Sun} is the averaged value calculated for A* – B^s.

Outdoor test	P_{Sun} in A* /(Wm^{-2})	P_{Sun} in B^s /(Wm^{-2})	T_s /(°C)	T_g in B^s (°C)	T_v in B^s /(°C)	α_{Sun}
#1	910	921	308	56	59	0.930
#2	910	885	302	54	59	0.915
#3	906	897	305	50	58	0.910
#4	923	942	306	56	60	0.915
#5	915	926	311	50	59	0.932
#6	923	943	313	51	60	0.909

$\bar{\alpha}_{Sun-Opt} = 0.933 \pm 0.003$

Table 1 summarises the experimental results of the six outdoor tests. It has been reported P_{Sun} at A* and B^s, that is, at the start and end of the interval were used to measure α_{Sun}. The absorber, glass, and vacuum chamber temperatures (T_s, T_g and T_v) measured at stagnation are also reported. The last column shows the mean value of the calculated α_{Sun} of the interval A* – B^s. In the last line of the table $\alpha_{Sun-Opt}$ is also shown. The six runs were conducted on clear-sky days in Naples (40° 51' N – 14° 18' E) in October 2020 around noon. The chamber was then exposed to sunlight and ambient air. There is a good agreement between the six calorimetric measurements and the optical measurements, with a maximum discrepancy of 0.024, corresponding to 2.5% of $\alpha_{Sun-Opt}$. Considering all calorimetric measurements as equivalent, we can calculate the average value of α_{Sun} and its standard deviation as $\bar{\alpha}_{Sun} = 0.92 \pm 0.01$, which agrees with $\alpha_{Sun-Opt} = 0.933 \pm 0.003$

Table 2. Summary of six indoor calorimetric experiments. The table shows the control voltage of the LED system and the corresponding P_{LED}, the temperatures at the stagnation of the absorber, glass, and vacuum chamber, T_s, T_g and T_v, respectively. α_{LED} for each test is reported. α_{LED} is the averaged value calculated for A* – B^s. The last line reports $\alpha_{LED-Opt}$ and the α_{LED} averaged over all six measurements.

Indoor test	Control Voltage /V	P_{LED} /(Wm^{-2})	T_s /(°C)	T_g in B^s /(°C)	T_v in B^s /(°C)	α_{LED}
#1	6.50	1060	330	49	48	0.944
#2	5.80	981	318	46	38	0.928
#3	5.57	951	320	70	55	0.929
#4	4.00	715	289	66	58	0.949
#5	3.00	552	263	60	53	0.946
#6	2.00	392	226	49	44	0.940

$\alpha_{LED-Opt} = 0.947 \pm 0.003$ $\bar{\alpha}_{LED} = 0.939 \pm 0.009$

Table 2 is analogous to Table 1 but refers to the six indoor runs carried out with the LED system. For this reason, P_{LED} is identified by a single value, which is constant throughout the warm-up phase, whereas the Sun's irradiance intrinsically fluctuates. Each P_{LED} is coupled to a control voltage, which is the electric potential driving the control electronics of the LED system and ranges between 2 and 10 V (D'Alessandro et al., 2021). Indoor runs #1 and #2 have glass and vacuum chamber temperatures that are sensibly lower than for run #3 because of the presence of an external fan for cooling the chamber walls. Although the difference was approximately 20 °C, the resulting α_{LED} exhibited no relevant change. Indoor runs #4, #5, and #6 were performed at a lower P_{LED} to obtain lower T_s. In this case, no significant variations in α_{LED} could be detected. A comparison of the α_{LED} estimations obtained under different conditions reveals a good agreement with the optically evaluated absorptance $\alpha_{LED-Opt}$ reported in Table 2. The difference between the

average α_{LED} ($\bar{\alpha}_{LED}$ = 0.939 ± 0.009) and $\alpha_{LED\text{-}Opt}$ (0.947±0.003) was slightly smaller than in the direct sun illumination case, which could be due to the high temporal stability of the LED system.

The good agreement between the calorimetric and optical absorptance measurements globally validated our model and procedures. In particular, it confirms the appropriate modelling of the thermal losses in Eq. 11, as ε_{etF} can be used to correctly estimate the losses during the warm-up phase and it also validates the assumption of a temperature and power independent absorptance α_l. The proposed model and equipment can measure the thermal emittance and solar absorptance of selective solar absorbers with a precision higher that 0.004 and 0.01, respectively. The larger error in the solar absorptance is essentially due to the 1% calibration error of the chosen pyranometer, which influences the incident power estimation.

6. Conclusion

We presented a novel method and experimental setup based on a power balance equation for estimating the optical properties of a flat selective absorber under high vacuum up to the stagnation temperature. These are appropriate conditions for assessing the performance of HVFPs. Optical measurements of the surface reflectivity were performed at room temperature of both sides of a commercial absorber sample. Outdoor and indoor (using a solar simulator) calorimetric measurements were conducted using the same commercial absorber (Mirotherm from Alanod) and the results were compared.

The effective thermal emittance of the sample, when measured calorimetrically, was not dependent on the test conditions. Outdoor runs returned the same results as those obtained indoors under controlled ambient conditions (with and without external fan cooling of the chamber, and incident light power on the cover glass ranging between 1 kWm^{-2} and 0.4 kWm^{-2}). All measured effective thermal emittances are contained within a variation of ±0.0035 for an absorber temperature below 150 °C and within ±0.0025 for above. These values correspond to 4% and 2.5% of the measured emittance, respectively.

The sum of the optically evaluated thermal emittances of both sides of the absorber was in good agreement with the effective thermal emittance calorimetrically estimated for temperatures below 150 °C. Above this threshold, the mathematical correction of the optical properties of the absorber based on the hypothesis of infinite plates fails. It results in a discrepancy of -11% at 50 °C which is reduced to -8% at 300 °C, underestimating the calorimetric results over the entire investigated temperature range. Such differences correspond to an error in the emitted power calculation of about 60 Wm^{-2} at 300 °C. The measured light absorptance agreed with that obtained from the optical measurements in both outdoor and indoor tests with a maximum variation of 2.5%.

The emissivity discrepancies measured for the Mirotherm samples highlight the importance of measuring the radiative properties of an absorber up to high temperatures and under high vacuum to correctly assess the performance of selective solar absorbers, especially those developed for HVFPs.

7. Acknowledgments:

References

Arya, F., Moss, R., Hyde, T., Shire, S., Henshall, P., Eames, P., 2018a. Vacuum enclosures for solar thermal panels Part 1: Fabrication and hot-box testing. Solar Energy 174, 1212–1223. https://doi.org/10.1016/j.solener.2018.10.064

Arya, F., Moss, R., Hyde, T., Shire, S., Henshall, P., Eames, P., 2018b. Vacuum enclosures for solar thermal panels Part 2: Transient testing with an uncooled absorber plate. Solar Energy 174, 1224–1236. https://doi.org/10.1016/j.solener.2018.10.063

Beikircher, T., Benz, N., Spirkl, W., 1995. Gas Heat Conduction in Evacuated Flat-Plate Solar Collectors: Analysis and Reduction. Journal of Solar Energy Engineering 117, 229–235. https://doi.org/10.1115/1.2847807

Benvenuti, C., 2013. The SRB solar thermal panel. Europhysics News 44, 16–18. https://doi.org/10.1051/epn/2013301

Benz, N., Beikircher, T., 1999. HIGH EFFICIENCY EVACUATED FLAT-PLATE SOLAR COLLECTOR FOR PROCESS STEAM PRODUCTION1Paper presented at the ISES Solar World Congress, Taejon, South Korea, 24–29 August 1997.1. Solar Energy 65, 111–118. https://doi.org/10.1016/S0038-092X(98)00122-4

Buonomano, A., Calise, F., d'Accadia, M.D., Ferruzzi, G., Frascogna, S., Palombo, A., Russo, R., Scarpellino, M., 2016. Experimental analysis and dynamic simulation of a novel high-temperature solar cooling system. Energy Conversion and Management 109, 19–39. https://doi.org/10.1016/j.enconman.2015.11.047

CREE, 2014. CREE XLamp CXA3590 LED [WWW Document]. XLampQR CXA3590 LED Datasheet. URL www.cree.com/Xlamp

D'Alessandro, C., De Maio, D., Mundo, T., Musto, M., Di Giamberardino, F., Monti, M., Dalena, D., Palmieri, V.G., De Luca, D., Di Gennaro, E., Russo, R., 2021. Low cost high intensity LED illumination device for high uniformity solar testing. Solar Energy 221, 140–147. https://doi.org/10.1016/j.solener.2021.04.017

De Maio, D., D'Alessandro, C., Caldarelli, A., De Luca, D., Di Gennaro, E., Russo, R., Musto, M., 2021a. A Selective Solar Absorber for Unconcentrated Solar Thermal Panels. Energies 14, 900. https://doi.org/10.3390/en14040900

De Maio, D., D'Alessandro, C., Caldarelli, A., De Luca, D., Gennaro, E.D., Casalino, M., Iodice, M., Gioffre, M., Russo, R., Musto, M., 2021b. Multilayers for efficient thermal energy conversion in high vacuum flat solar thermal panels. Thin Solid Films 735, 138869. https://doi.org/10.1016/j.tsf.2021.138869

Dushman, S., Research Staff of General Electric Research Laboratory, Brown, S.C., 1949. Scientific Foundations of Vacuum Technique. American Journal of Physics.

Echániz, T., Setién-Fernández, I., Pérez-Sáez, R.B., Prieto, C., Galindo, R.E., Tello, M.J., 2015. Importance of the spectral emissivity measurements at working temperature to determine the efficiency of a solar selective coating. Solar Energy Materials and Solar Cells 140, 249–252. https://doi.org/10.1016/j.solmat.2015.04.009

Farjana, S.H., Huda, N., Mahmud, M.A.P., Saidur, R., 2018. Solar process heat in industrial systems – A global review. Renewable and Sustainable Energy Reviews 82, 2270–2286. https://doi.org/10.1016/j.rser.2017.08.065

Gao, D., Gao, G., Cao, J., Zhong, S., Ren, X., Dabwan, Y.N., Hu, M., Jiao, D., Kwan, T.H., Pei, G., 2020. Experimental and numerical analysis of an efficiently optimized evacuated flat plate solar collector under medium temperature. Applied Energy 269, 115129. https://doi.org/10.1016/j.apenergy.2020.115129

Gorjian, S., Ebadi, H., Calise, F., Shukla, A., Ingrao, C., 2020. A review on recent advancements in performance enhancement techniques for low-temperature solar collectors. Energy Conversion and Management 222, 113246. https://doi.org/10.1016/j.enconman.2020.113246

Howell, J.R., Mengüç, M.P., Daun, K.J., Siegel, R., 2021. Thermal radiation heat transfer, Seventh edition. ed. CRC Press / Taylor & Francis Group, Boca Raton.

Ismail, M.I., Yunus, N.A., Hashim, H., 2021. Integration of solar heating systems for low-temperature heat demand in food processing industry – A review. Renewable and Sustainable Energy Reviews 147, 111192. https://doi.org/10.1016/j.rser.2021.111192

Jyothi, J., Soum-Glaude, A., Nagaraja, H.S., Barshilia, H.C., 2017. Measurement of high temperature emissivity and photothermal conversion efficiency of TiAlC/TiAlCN/TiAlSiCN/TiAlSiCO/TiAlSiO spectrally selective coating. Solar Energy Materials and Solar Cells 171, 123–130. https://doi.org/10.1016/j.solmat.2017.06.057

Kraemer, D., McEnaney, K., Cao, F., Ren, Z., Chen, G., 2015. Accurate determination of the total hemispherical emittance and solar absorptance of opaque surfaces at elevated temperatures. Solar Energy Materials and Solar Cells 132, 640–649. https://doi.org/10.1016/j.solmat.2014.10.026

Le Baron, E., Raccurt, O., Giraud, P., Adier, M., Barriga, J., Diaz, B., Echegut, P., De Sousa Meneses, D., Capiani, C., Sciti, D., Soum-Glaude, A., Escape, C., Jerman, I., López, G.A., Echániz, T., Tello, M.J., Matino, F., Maccari, A., Mercatelli, L., Sani, E., 2019. Round Robin Test for the comparison of spectral emittance measurement apparatuses. Solar Energy Materials and Solar Cells 191, 476–485. https://doi.org/10.1016/j.solmat.2018.11.026

Masuda, H., Higano, M., 1985. Transient calorimetric technique for measuring total hemispherical emissivities of metals with rigorous evaluation of heat loss through thermocouple leads. J. Opt. Soc. Am. A 2, 1877. https://doi.org/10.1364/JOSAA.2.001877

Mercatelli, L., Meucci, M., Sani, E., 2015. Facility for assessing spectral normal emittance of solid materials at high temperature. Appl. Opt. 54, 8700. https://doi.org/10.1364/AO.54.008700

Moss, R., Shire, S., Henshall, P., Arya, F., Eames, P., Hyde, T., 2018. Performance of evacuated flat plate solar thermal collectors. Thermal Science and Engineering Progress 8, 296–306. https://doi.org/10.1016/j.tsep.2018.09.003

Niranjan, K., Soum-Glaude, A., Carling-Plaza, A., Bysakh, S., John, S., Barshilia, H.C., 2021. Extremely high temperature stable nanometric scale multilayer spectrally selective absorber coating: Emissivity measurements at elevated temperatures and a comprehensive study on ageing mechanism. Solar Energy Materials and Solar Cells 221, 110905. https://doi.org/10.1016/j.solmat.2020.110905

Pranesh, V., Velraj, R., Christopher, S., Kumaresan, V., 2019. A 50 year review of basic and applied research in compound parabolic concentrating solar thermal collector for domestic and industrial applications. Solar Energy 187, 293–340. https://doi.org/10.1016/j.solener.2019.04.056

Tian, M., Su, Y., Zheng, H., Pei, G., Li, G., Riffat, S., 2018. A review on the recent research progress in the compound parabolic concentrator (CPC) for solar energy applications. Renewable and Sustainable Energy Reviews 82, 1272–1296. https://doi.org/10.1016/j.rser.2017.09.050

Tian, Y., Zhao, C.Y., 2013. A review of solar collectors and thermal energy storage in solar thermal applications. Applied Energy 104, 538–553. https://doi.org/10.1016/j.apenergy.2012.11.051

TVP Solar SA, 2017. MT-Power: Thermal Applications 100°C To 180°C.

Vengadesan, E., Senthil, R., 2020. A review on recent developments in thermal performance enhancement methods of flat plate solar air collector. Renewable and Sustainable Energy Reviews 134, 110315. https://doi.org/10.1016/j.rser.2020.110315

Verma, S.K., Gupta, N.K., Rakshit, D., 2020. A comprehensive analysis on advances in application of solar collectors considering design, process and working fluid parameters for solar to thermal conversion. Solar Energy 208, 1114–1150. https://doi.org/10.1016/j.solener.2020.08.042

Willrath, H., Gammon, R.B., 1978. The measurement of optical properties of selective surfaces using a solar calorimeter. Solar Energy 21, 193–199. https://doi.org/10.1016/0038-092X(78)90021-X